Mechanism of magnetic heating in Mn-doped magnetite nanoparticles and the role of intertwined structural and magnetic properties

(Article begins on next page)

15 October 2024

Mechanism of magnetic heating in Mn-doped magnetite nanoparticles and role of the intertwined structural and magnetic properties

L. Del Bianco[1]*, F. Spizzo[1], G. Barucca[2], M. R. Ruggiero[3], S. Geninatti Crich[3], M. Forzan[4], E. Sieni[4], P. Sgarbossa[4]

[1] Dipartimento di Fisica e Scienze della Terra, Università di Ferrara, I-44122 Ferrara, Italy

[2] Dipartimento SIMAU, Università Politecnica delle Marche, I-60131 Ancona, Italy

[3] Dipartimento di Biotecnologie Molecolari e Scienze per la Salute, Università di Torino, I-10126 Torino, Italy

[4] Dipartimento di Ingegneria Industriale, Università di Padova, I-35131 Padova, Italy

*Corresponding author. E-mail address: lucia.delbianco@unife.it

Abstract

We study the mechanism of heat generation, induced by an alternating magnetic field, in magnetite nanoparticles doped with manganese, produced by thermal decomposition from organometallic precursors. We investigate a set of four samples obtained by varying the duration of the reflux treatment carried out at the temperature of 300 °C during the synthetic procedure. On increasing this parameter from 60 to 180 minutes, the mean size of the nanoparticles increases, though remaining below 10 nm, as well as the saturation magnetization, which in all the samples, thanks to the Mn doping, is higher than in magnetite nanoparticles taken as a reference. The combination of these two events has two main consequences. First, it determines the intensity of the dipolar interactions between the nanoparticles, thus influencing their magnetic relaxing behavior, which, in turn, is closely related to the heating efficiency. Secondly, in a heating test, it is possible to operate in the regime of non-linear magnetic response of the nanoparticles at values of amplitude and frequency of the alternating field usually employed for biomedical applications. We show that, in this regime, the Specific Absorption Rate (SAR) in each sample depends linearly on the fraction of nanoparticles that are not superparamagnetic. This opens to the possibility of modulating the heating capacity of the produced nanoparticles, so as to match specific needs, changing only a single synthesis parameter and opportunely exploiting the strict connection between structural features, magnetic properties and measurement conditions.

Introduction

The use of magnetic nanoparticles (NPs) for nanomedicine applications is a fast-growing research field due to their potential as diagnostic and therapeutic agents. [1, 2, 3, 4] One of the most investigated phenomena is magnetic hyperthermia, which refers to the production of heat obtained by subjecting the NPs to an alternating magnetic field. [5, 6, 7, 8, 9] The effect can be exploited in the cancer treatment, to raise the temperature at the tumor site above the systemic one, or to induce a controlled drug release through the thermal stimulus. [10, 11, 12, 13, 14, 15]

The heat generated by the NPs during one cycle of the magnetic field corresponds to the area of the resulting hysteresis loop. [16] Therefore, fundamental magnetic parameters are the anisotropy and the saturation magnetization M_S, which directly determine the hysteretic behavior. [17] A key ingredient is the volume V of the NPs, which influences their magnetization pattern and the magnetization reversal mode. [18, 19] Moreover, the loop area depends on the frequency (f_m) and amplitude (H_{max}) of the applied field and on the temperature (T). [20] All these parameters are involved and strictly intertwined in the relaxation of the NPs magnetization. The relaxing behavior affects the hysteresis phenomenon to the point of causing its complete disappearance when the thermal energy becomes comparable to the anisotropy energy barrier for magnetization reversal (superparamagnetism). [21, 22]

This article deals with magnetite NPs, doped with manganese for the preliminary purpose of improving M_S. NPs suitable for biological applications must be biocompatible and currently only spinel iron oxides (magnetite and maghemite) satisfy this requirement to an acceptable extent. However, the magnetization of iron oxide NPs is often reported to be lower than that of the bulk phase, due to the canting of the spins located at the surface and/or in the core, caused by a reduced coordination and broken superexchange bonds. [23, 24, 25, 26, 27] This is detrimental to the heating efficiency. To get around this problem, preserving the biocompatibility, Mn-doped magnetite NPs appear particularly promising since the substitution of Fe^{2+} ions with Mn^{2+} ions in the Fe_3O_4 structure may lead to the enhancement of M_S. Giri et al. prepared $Fe_{1-x}Mn_xFe_2O_4$ NPs (mean size ~ 10-12 nm) by a co-precipitation method and studied the heating efficiency by calorimetric measurement in a field with f_m = 300 kHz and H_{max} = 10 – 45 kA/m. They found out that the Specific Absorption Rate parameter (SAR) and M_S showed a similar dependence on the Mn concentration, reaching maximum values for x = 0.4 (M_S ~ 85 emu/g and SAR~ 30 W/g ferrite). [28] J. Jang et al. prepared 15nm-sized $(Zn_xMn_{1-x})Fe_2O_4$ NPs by a one-pot thermal decomposition method; for x = 0.4, they reported M_S = 175 emu/g(Zn+Mn+Fe) and SAR = 432 W/g(Zn+Mn+Fe) (f_m and H_{max} were 500 kHz and 3.7 kA/m, respectively). [29] The same group also prepared $MnFe_2O_4$ NPs with mean size 15 nm and M_S = 125 emu/g(magnetic atoms) and measured a SAR = 411 W/g(magnetic atoms) at f_m = 500 kHz and H_{max}

= 37.3 kA/m.[8] R. Otero-Lorenzo et al. prepared Mn-doped iron oxide NPs of 8-9 nm in size, by a solvothermal method, having room-temperature M_S = 66 emu/g and SAR ~ 73 W/g per mass of Fe+Mn (f_m and H_{max} of 183 kHz and 17 kA/m, respectively). [30] Casula et al. studied Mn-doped iron oxide NPs arranged into flower-like structures of ~ 50 nm in size, prepared by a chemical decomposition method. For f_m = 300 kHz and H_{max} varying between 12 and 24 kA/m, SAR values ranging between 200 and 400 W/g(Fe+Mn) were measured, in spite of the reported oddly low M_S ~ 40 emu/g. [31] On the contrary, a remarkably high M_S = 89.5 emu/g was measured by L. Yang et al. in Mn-doped NPs (mean size ~ 18 nm), studied with the aim of developing high-performance magnetic resonance contrast agents.[32] Indeed, great care should be taken when comparing M_S and SAR (or SLP, specific loss power) values. In fact, different conventions can be adopted regarding the normalization to the mass of the sample, since some researchers are used to consider the mass of the magnetic ferrite phase (possibly corrected for the presence of non-magnetic components, such as surfactants), [5, 28, 33, 34] whereas others researchers are used to normalize to the weight of the metallic atoms. [30, 31] Moreover, in order to be comparable, SAR values estimated using a calorimetric method should refer to measurements carried out not only at the same f_m and H_{max}, but also in similar thermodynamic conditions and the NPs should be dispersed at a similar concentration and in the same solvent. At present, the wide variety of custom instruments and the lack of standardized protocols for hyperthermia measurements makes the comparison between SAR measurements very difficult and often impossible. [34, 35]

We report about selected samples of NPs obtained by varying the duration (60 ÷180 minutes) of the reflux treatment at 300 °C, carried out during a thermal decomposition synthetic procedure, based on the method developed by S. Sun et al..[36] The mean size of the NPs increases with increasing the holding time at 300 °C - though remaining below 10 nm – as well as M_S, thus fulfilling our preliminary goal. The combination of these two events produces a chain of concatenated effects. In fact, it results in enhanced dipolar magnetic interactions between the NPs. In turn, the presence of dipolar interactions gives rise to an effective magnetic anisotropy, which rules the magnetic relaxation time. The dipolar interactions also affect the Brownian rotation motion that the NPs undergo when dispersed in a fluid. [20]

To elucidate these connections, in the first part of this article the evolution of the structural and magnetic properties of the NPs (in form of powder and of ferrofluid, in n-octane) is investigated in depth. Then, the study of the magnetic heating mechanism of the NPs, in form of ferrofluid, is addressed. Apart from a few exceptions, [6, 16, 37, 38] most studies on the heating properties of magnetic NPs refer to the linear response theory (LRT), which assumes that the magnetization of the NPs

depends linearly on the magnetic field.[20] According to LRT, the hysteresis loop area is null when the NPs are in the full superparamagnetic and blocked regimes and reaches a maximum at the transition. Actually, the LRT model can be used providing that the parameter $\zeta = M_S V H_{max}/k_B T < 1$ (k_B, Boltzmann constant).[16, 39] In our samples, for values of f_m and H_{max} of the same order of those generally used in clinical applications,[40] $\zeta > 1$. In this condition, the heating efficiency changes substantially from sample to sample and we show that the SAR parameter depends linearly on the fraction of NPs that are not in the superparamagnetic regime. The size distribution of the NPs and M_S – both tuned through a single synthesis parameter, i.e. the reflux time at 300 °C – determine, through a sort of *domino* effect mediated by dipolar interactions, the heating efficiency of the NPs, which is remarkably high in those obtained for a reflux time of 180 minutes. This opens new perspectives for controlling on demand the magnetic heating phenomenon, according to specific needs.

2. Experimental

2.1 Synthesis of the nanoparticles

The samples of Mn-doped magnetite NPs are prepared by thermal decomposition from organometallic precursors.[36] To this end, 2.12 g of iron(III) acetylacetonate ([Fe(acac)$_3$]), 0.76 g of manganese(II) acetylacetonate ([Mn(acac)$_2$]), 5.98 g of oleylamine, 5.72 g of oleic acid, and 6.91 g of 1,2-tetradecanediol are dissolved in 60 mL of diphenyl ether. Hence, the Mn/Fe atomic ratio in the reaction mixture is 0.5. The obtained solution is heated at 200°C for 2 hours and then refluxed at 300°C for a time varying between 1 and 3 hours, under inert atmosphere (N$_2$). The temperature of 300°C is chosen to ensure the thermal decomposition of both the metal acetylacetonate complexes (around 180°C for [Fe(acac)$_3$] and 250°C for [Mn(acac)$_2$]).

After cooling to room temperature, the NPs are precipitated by treating the dark suspension with a twofold volume of ethanol, separated magnetically, washed twice with ethanol, dried under vacuum, and stored as a black powder. The oleate-coated NPs can be easily dispersed in apolar solvents (e.g. alkanes).

All the reagents and solvents have been purchased from Sigma-Aldrich and used without further purification.

Here, we report about a set of four samples of NPs, labelled SA, SB, SC and SD, differing for the duration of the treatment at 300 °C: 60, 100, 150 and 180 minutes, respectively (we call this parameter 't300'). For each type of analysis, we will specify whether the NPs are in form of powder or of ferrofluid, namely dispersed in n-octane at a concentration of 10 mg/mL. It is worth remarking that the magnetic measurements on the ferrofluids are carried out at a temperature lower than the melting

temperature of octane (216 K). Also in this case, we will often use the word 'ferrofluid' to refer to the NPs in octane and to distinguish them from those in powder form, with no regard to the fact that the octane is in the frozen state, actually.

2.2 Characterization techniques

The size distribution and inner structure of the NPs is investigated by transmission electron microscopy techniques (TEM) by using a Philips CM200 microscope operating at 200 kV and equipped with a LaB_6 filament. For TEM observations, a small quantity of NPs is dispersed in n-hexane and subjected to ultrasonic agitation for approximately one minute. A drop of the suspension is deposited on a commercial TEM grid covered with a thin carbon film; finally, the grid is kept in air until complete evaporation of the n-hexane.

The amount of Fe and Mn in the NPs is assessed by using inductively coupled plasma mass spectrometry (ICP-MS; element-2; Thermo-Finnigan, Rodano (MI), Italy). Sample digestion is performed by dissolving 2 mg of each powder in concentrated HNO_3 (70%, 1 mL) under microwave heating (Milestone MicroSYNTH Microwave Labstation).

Dynamic light scattering (DLS) measurements are carried out on the Mn-doped magnetite NPs using a Malvern Zetasizer 3000HS (Malvern, U.K.); the samples are analyzed at 25 °C in n-octane after being subjected to ultrasonication.

Thermogravimetric (TGA) measurements are conducted on the NPs in form of powder in nitrogen purge gas from 50 °C to 600 °C (heating rate = 10 °C/min). The instrument is also equipped to perform TGA measurements in a magnetic field gradient, allowing the detection of magnetic transitions.

X-ray diffraction (XRD), Energy dispersive X-ray spectrometry (EDS) and Fourier transform infrared spectroscopy (FT-IR) analyses are also carried out and the related experimental methods are described in the Electronic Supplementary Information Section.

The magnetic properties are studied using a Quantum Design superconducting quantum interference device (SQUID) magnetometer. The instrument measures the magnetic moment of samples, both in solid or in liquid form, as a function of magnetic field (maximum applied field 50 kOe) and of temperature T (5-300 K temperature range).

The heating properties of the Mn-doped magnetite NPs in an alternating magnetic field are tested using a custom-made apparatus equipped with a 7-turns inductor, 8 cm internal diameter, 15 cm long, supplied by an EASYHEAT L1 5060 10.0 kW (Ambrell) generator, as described elsewhere;[41] the temperature is measured by means of a fiber optic thermometer, Optocom Fotemp-1H thermometer with a TS3/2 fiber optic.

3. Results and discussion

3.1 Structural properties and formation of the nanoparticles

A TEM analysis is conducted on the four samples of NPs. In Fig. 1 bright field TEM images, also in high-resolution mode (HRTEM), are shown for samples SA, SB and SD, which are representative of different steps of the process of formation of the NPs.

The SA NPs appear widely size-distributed and disorderly arranged on the carbon film of the TEM grid (Fig. 1a). HRTEM observations reveal that many of the SA NPs are not single crystals, but consist of two or more small grains (Fig. 1d), which can account for the observed variety of irregular shapes. With increasing t300, the NPs become progressively more uniform in size and shape and this favors the observed tendency to self-order on the carbon film (Fig. 1b,c). This last behavior is also consistent with the presence of a more homogeneous layer of oleate around the NPs, which impedes the intimate contact between them. In Fig. 1c, relative to SD, the distance between the NPs, in the regions where they are more regularly arranged, is ~ 3 nm, which is less than the two times the length of the oleic acid molecule (~ 2.5 nm).[42] This indicates that the oleate chains on one NP interact with those on the neighboring ones, as observed also by other researchers in magnetite NPs produced by thermal decomposition.[43]

Selected area electron diffraction (SAED) measurements are performed on the samples in similar experimental conditions. Typical SAED patterns for SA, SB and SD are shown in the insets of Fig.1a-c, respectively. They are composed of continuous rings, consistent with the random orientation of the NPs. The number and intensity of the rings are similar for the samples SA and SD, indicating a good level of crystallinity of the NPs. The same cannot be said for the SB NPs whose diffraction pattern shows less intense rings and diffuse intensity among them, which suggests a lower degree of crystallinity. This last statement is confirmed by HRTEM observations, as displayed in Fig. 1e: the atomic planes are clearly visible inside the core of the NP whereas amorphous material is present at the surface (arrowed). The same feature is not observed in the SA and SD NPs since the atomic planes are well visible in all their extension (Fig. 1d,f).

The distribution in size (D) of the NPs is obtained through the analysis of bright field TEM images. A population of about 300 NPs for each sample, including SC, is investigated. We consider that the physical size of the NPs coincides with their magnetic size since the oleate coating produces a weak TEM contrast and it is substantially not visible by TEM. The results are shown in Fig. 2, together with the corresponding values of mean size D_{ave} (also reported in Table 1) and standard deviation σ. On increasing t300, D_{ave} increases and the distribution shrinks.

The HRTEM results allow one to draw the following picture on the evolution of the NPs structure during the synthesis reaction. Initially small crystallites form, which tend to coalesce, as observed in SA. Going on with the reaction, a mechanism similar to the Ostwald ripening intervenes, namely the smaller NPs dissolve and the material deposits onto the larger ones. The shift to the right of the size distributions and the increase in D_{ave} with increasing t300 support this description (Fig. 2). This mechanism leads to the formation of the layer of disordered amorphous-like material around the crystalline cores of the SB NPs. Then, the crystallinity of the NPs improves passing from SB to SD and the SD NPs are mostly single crystals.

3.2 Compositional properties

The diffraction rings in the SAED patterns shown in Fig.1 correspond to the following interplanar distances: (0.298 ± 0.003) nm, (0.252 ± 0.003) nm, (0.210 ± 0.002) nm, (0.172 ± 0.002) nm, (0.161 ± 0.002) nm, (0.148 ± 0.001) nm and (0.128 ± 0.001) nm. These values are in good agreement with diffraction data reported for magnetite ('International Centre for Diffraction Data'—ICDD card n. 19-0629). Moreover, HRTEM images of the NPs are analyzed by using the Gatan Microscopy Suite GMS3 software [44], which allows the fast Fourier transform (FFT) of the image. The subsequent analysis, in terms of geometry and interplanar distances, of the obtained FFT pattern confirms that all the NPs have a ferrite cubic spinel structure. No other phase is detected by SAED measurements and HRTEM observations. These analyses cannot provide evidence of Mn doping in the NPs because Fe_3O_4 and $MnFe_2O_4$ are isostructural phases and the differences in the values of the interplanar distances are smaller than the experimental error. The XRD analysis carried out on all the samples confirms these conclusions. As an example, the spectrum for sample SD is shown in the Electronic Supplementary Information Section (Fig. S1): the broad reflection peaks correspond to the spinel structure of magnetite.

However, the presence of Mn in the NPs is assessed by ICP-MS elemental analysis. The ratio between the atomic content of Mn and Fe is (0.18 ± 0.03) in SA, (0.16 ± 0.04) in SB, (0.20 ± 0.03) in SC and (0.19 ± 0.03) in SD, namely is the same in all the samples within the errors. The EDS analysis, described in the Electronic Supplementary Information Section, provides Mn/Fe = (0.22 ± 0.06) for SD (Fig. S2) and equal values, within the errors, for the other samples. For all samples, the ICP-MS and EDS results are consistent, but the latter ones are affected by a larger experimental error. Hence, despite the final NPs do not retain the Mn/Fe ratio of the initial metal precursors - which may be ascribed to the different decomposition temperatures of the two metal acetylacetonate complexes [30, 45] - the average composition of the NPs does not vary with increasing the reflux time, in the chosen reaction conditions.

The FT-IR investigation provides spectra similar for all the NPs, confirming the presence of the oleate that surrounds the NPs (bands at 1410 cm^{-1} for C-H$_{rock.}$, 1543 cm^{-1} for C=C$_{stretch.}$, 2850-2920 cm^{-1} for C-H$_{stretch.}$ and 3370 cm^{-1} for the residual O-H$_{stretch}$) and of the iron oxide phase (bands at 392 and 573 cm^{-1}). No other signal is visible. As an example, the spectrum for sample SA is reported in the Electronic Supplementary Information Section (Fig. S3).

TGA measurements are carried out on the NPs in form of powder in order to measure the mass loss caused by the decomposition of the oleate, which occurs between 300°C and 500 °C (Fig. S4 in the Electronic Supplementary Information). The weight fraction of oleate in the samples, estimated in this way, is reported in Table 1. The fraction of oleate around the NPs tends to reduce with increasing D$_{ave}$, reasonably due to the corresponding decrease of the surface/volume ratio of the NPs.[46, 47]

TGA measurements are also carried out in a magnetic field gradient. In Fig. 3a we compare the curves measured with and without gradient on a reference sample, called SRef, consisting of NPs of Fe$_3$O$_4$. These NPs of pure magnetite are produced by thermal decomposition, namely through the same synthesis method described in Section 2.1. Obviously, only the [Fe(acac)$_3$] precursor is used in this case. This difference strongly affects the reaction kinetics and we have observed that, compared to the Mn-doped NPs, different morphological and structural properties are attained as a function of t300, even keeping all the other synthesis parameters unchanged. Hence, as a benchmark for the TGA analysis and for the analysis of M$_S$, reported later, we have selected, among different types of NPs of magnetite that we have prepared, that with the highest M$_S$. The mean size of this NPs, estimated by TEM, is D$_{ave}$ ~ 9 nm (Table 1). The curve measured with the magnetic gradient features an upward step, not present in the curve measured without gradient, which corresponds to the ferrimagnetic-paramagnetic transition. The Néel temperature T$_N$ = (583±1) °C is very close to the nominal value of bulk magnetite (585 °C). The TGA curves with magnetic gradient for the Mn-doped magnetite NPs are shown in Fig. 3b. Due to the Mn doping, T$_N$ is well below that measured in SRef (~ 60-70 °C lower) and it decreases with increasing t300. No particular feature is visible in correspondence to T$_N$ of Fe$_3$O$_4$ or of MnFe$_2$O$_4$ (300 °C), which is in favor of a uniform Mn doping of the NPs. We also observe that the magnetic transition is less sharp in SB and SC compared to the other two samples. This is consistent with a lower crystallinity degree, as also confirmed by the HRTEM analysis.

3.3 Saturation magnetization

Magnetic hysteresis loops are measured on the dried Mn-doped magnetite NPs at different temperatures T in the 5-300 K range. The loops at T = 5 K are shown in Fig. 4a. In particular, the specific magnetization (M) is reported, obtained by dividing the magnetic moment, measured by SQUID, for the mass of the magnetic NPs (hence, it is expressed in emu/g). The latter quantity is

calculated by subtracting from the whole sample mass that of the oleate estimated by TGA (Table 1). The values of the saturation magnetization M_S are extrapolated from the loops for 1/H tending to zero; the values at T = 5 and 300 K are reported in Table 1. In Fig. 4b the curves of M_S vs. T are shown for all the samples, including SRef.

Magnetite shows an inverse spinel structure in which the trivalent ions Fe^{3+} (bearing a magnetic moment of 5 μ_B) are equally distributed in the tetrahedral (A) and octahedral (B) sites and the divalent ions Fe^{2+} (bearing a magnetic moment of 4 μ_B) are placed in the B sites, according to the notation $[Fe^{3+}]_A[Fe^{2+} Fe^{3+}]_B O_4$. A net magnetic moment arises from the Fe^{2+} ions since the contributions from the Fe^{3+} ions annihilate reciprocally, being the superexchange interaction between A and B sites antiferromagnetic in nature. Hence, the predicted magnetic moment per unit cell is 4 μ_B and at T = 0 K M_S = 98 emu/g. [17]

The $MnFe_2O_4$ phase adopts a mixed spinel structure in which both the Fe^{3+} ions and the Mn^{2+} (isoelectronic with Fe^{3+} and, hence, with a magnetic moment of 5 μ_B) are distributed between the A and B sites according to the notation $[Mn^{2+}_{1-x} Fe^{3+}_x]_A[Mn^{2+}_x Fe^{3+}_{2-x}]_B O_4$, being x the so-called inversion parameter. In the bulk phase, x $\sim$ 0.2, whereas values even larger than 0.5 have been found in NPs. [48, 49] Irrespective of x, the magnetic moment per unit cell of $MnFe_2O_4$ is 5 μ_B and, at T = 0 K, M_S = 112 emu/g. [17]

In Mn-doped magnetite, the substitution of Fe^{3+} ions with Mn^{2+} ions does not alter the net moment of the Fe_3O_4 unit. However, if the Mn^{2+} ions replace the Fe^{2+} ions, the low-temperature saturation magnetization of the material is expected to increase. This accounts for our results. In fact, in SRef, at T = 5 K M_S $\sim$ 73 emu/g, a value lower than M_S of bulk magnetite, as usually observed in NPs due to size effects such as spin canting. [26] A higher M_S is measured in all the samples of Mn-doped magnetite NPs. In particular, in the SA NPs, despite the mean size D_{ave} is well below that of SRef (Table 1), M_S $\sim$ 80 emu/g. M_S increases further in SB and SC and in the SD NPs, whose D_{ave} is similar to that of SRef, the remarkably high value of M_S $\sim$ 94 emu/g is measured. We think that this magnetization improvement on increasing t300 is not only ascribable to the increase in D_{ave}, which attenuates the spin canting effect, but also to the increase in the fraction of Mn^{2+} ions replacing Fe^{2+} ions in the B sites. In fact, the enhancement of M_S is accompanied by the T_N reduction, as shown in Fig. 4c. According to Yang et al.,[49] the value of T_N in Mn-ferrite NPs is uniquely governed by the inversion parameter, so that higher is the fraction of Mn^{2+} ions in the B sites and the lower is T_N, in line with our result.

M_S exhibits a stronger thermal dependence in the Mn-doped magnetite NPs than in sample SRef (Fig. 4b). It must be considered that the room-temperature M_S values for bulk Fe_3O_4 and $MnFe_2O_4$ are 92 emu/g and 80 emu/g respectively.[17] With reference to the values at T = 0 K, Ms undergoes a smaller percentage reduction in magnetite than in Mn-ferrite. Hence, the trend of M_S vs. T is strongly influenced by the Mn doping, as one can easily predict also considering that T_N of the Mn-doped magnetite NPs is much lower than that of SRef (Fig. 3). However, in all the samples of Mn-doped magnetite NPs, M_S at T = 300 K is larger than in SRef, up to ~ 19% in the case of SD. This is an important effect of the Mn doping. It is worth noticing that if we had produced $MnFe_2O_4$ NPs, probably we would have reached even higher values of Ms at T = 5 K compared to SRef, but not at T = 300 K. Indeed, there is no advantage in employing NPs of $MnFe_2O_4$ instead of Fe_3O_4 for room temperature applications, for which a high M_S is required.

Fig. 4d shows the curves of the coercivity H_C as a function of temperature. At T = 5 K, H_C is around 150-160 Oe in SA and SB and slightly higher in SC and SD (~ 190-200 Oe). A strong decrease of H_C between 5 K and 100 K is observed in all the samples. At T = 100 K, both H_C and the remanent magnetization M_r are annihilated in all samples except SD where magnetic hysteresis is measured even at T = 300 K. Magnetic loops are also measured on the samples in form of ferrofluids in the 5-50 K temperature range (Figs. S5 and S6 in the Electronic Supplementary Information). The thermal dependence of H_C and M_r is stronger than in the powders and no magnetic hysteresis is observed for T > 50 K.

3.4 Magnetic relaxation and effect of the magnetic interactions

The strong thermal dependence of H_C and M_r is consistent with a magnetic relaxing behavior of the assembly of NPs, possibly culminating in the superparamagnetic behavior when the thermal energy is comparable to the anisotropy energy barrier for the reversal of the magnetic moment of each NP. The Néel expression for the relaxation time of the magnetic moment is:

$$\tau_N = 1/f_0 \exp(KV/k_BT) \qquad (1)$$

where KV is the magnetic anisotropy energy barrier (K anisotropy coefficient, V volume of the NP), k_B the Boltzmann constant and f_0 the frequency factor.[21] The relation (1) assumes that the NP is a single domain in which the atomic spins rotate coherently. This is the so-called macrospin approximation that can be applied to the investigated NPs by virtue of their small size, which practically never exceeds 20 nm (Fig. 2).[19] Calling t_m the measuring time characteristic of the used investigating technique, the NP is in the superparamagnetic regime for $\tau_N < t_m$ (or for $f_m\tau_N < 1$, being

$f_m = 1/t_m$) and in the blocked ferromagnetic regime for $\tau_N > t_m$ ($f_m\tau_N > 1$). The transition between the two regimes occurs at $\tau_N = t_m$, i.e. $f_m\tau_N = 1$.

Accordingly, the temperature T_B (blocking temperature) above which an isolated ferromagnetic NP is superparamagnetic is expressed by the well-known relation:

$$T_B = KV/ k_B\ln(t_m f_0) \qquad\qquad (2)$$

A value of $\ln(t_m f_0) \sim 25$ is usually considered for SQUID measurements, which assumes $t_m = 100$ s ($f_m = 0.01$ Hz) and $f_0 = 10^9$ s^{-1}.[22]

In a NPs system, the possible existence of magnetic interactions leads to an increase of the anisotropy energy barriers of the NPs, which improves the thermal stability of their magnetization, shifting to higher temperature or preventing their entrance in the superparamagnetic regime.[21, 50, 51,52] Hence, one can consider that the NPs of the assembly are subjected to an effective magnetic anisotropy higher than their intrinsic anisotropy, namely the anisotropy that operates when they are isolated and that may include both the magnetocrystalline and the shape contributions. [27]

Information on the nature of magnetic interactions between the NPs in the investigated samples is obtained through the analysis of the ΔM plots.[53, 54, 55] For this purpose, measurements of isothermal remanent magnetization (IRM) and dc demagnetization remanence (DCD) are carried out, at T = 5 K, on the NPs dried and in form of ferrofluid, following a standard procedure in which the field is varied from 0 Oe up to 35 kOe. [27, 55] In Fig. 5, the parameter ΔM(H) = DCD(H)-[1- 2IRM(H)] is plotted as a function of H, both for the powders and for the ferrofluids. In all the cases, negative ΔM values are measured, which confirms the predominant presence of demagnetizing dipolar interactions.[22] The absolute peak value of ΔM can be used to assess the strength of the magnetic interactions. Hence, for each type of NPs, the dipolar interactions are much stronger in the powder than in the ferrofluid, which is perfectly reasonable.

To estimate the effective magnetic anisotropy to assign to the NPs, which rules their overall magnetic behavior, we consider the magnetic field value at which the hysteresis loop, measured at T = 5 K, closes (irreversibility field, H_{irr}), namely at which the descending and ascending branches join together.[56] H_{irr} can be considered as a measure of the anisotropy field of the system, i.e. $H_{irr} = 2K_{eff}/M_S$, where K_{eff} represents the effective anisotropy coefficient of the assembly of interacting NPs. In this relation, M_S must be expressed in (emu/cm^3). This requires that the values of M_S in Table 1 are multiplied by the density of the NPs. We consider the same density for the four samples and we assume that of bulk magnetite 5.1 g/cm^3. [57] H_{irr} and K_{eff} for the dried NPs and for the ferrofluids are reported in Table 2. The values of K_{eff} obtained in this way may be underestimated, actually. In fact,

due to the random orientation of the NPs anisotropy axes with respect to the field direction, H_{irr} is probably smaller than the anisotropy field of an amount difficult to indicate precisely.[58] Nevertheless, in all the samples K_{eff} is larger than the magnetocrystalline anisotropy coefficient of bulk magnetite, which is 1.1×10^5 erg/cm^3, [17] in spite of the Mn doping, which may possibly reduce the anisotropy, compared to pure magnetite.[28] For a given type of NPs, the value of K_{eff} in the powder is larger than that in the ferrofluid. This is in line with our expectation, also considering the results of the ΔM plots analysis (Fig. 5). Moreover, both in the powders and in the ferrofluids, K_{eff} increases with t300 since the mean size D_{ave} of the NPs and M_S increase.

The magnetothermal behavior of the NPs is investigated by measuring the magnetization for increasing temperature (heating rate = 3 K/min) in a static magnetic field H_{appl} = 20 Oe after cooling the samples from high temperature down to T = 5 K with no applied field (zero-field-cooling, ZFC) and in H_{appl} (field-cooling, FC). For the powders, the measurements are carried out in the 5-300 K temperature range; for the ferrofluids, the upper limit of the spanned temperature interval is 150 K, well below the melting temperature of octane, so that the NPs are not free to move. The obtained curves are shown in Fig. 6, as normalized to the value of M_{FC} at T = 5 K.

A magnetic irreversibility effect, i.e. a difference between the values of M_{FC} and M_{ZFC}, is visible in all the samples, confirming the presence of NPs whose magnetic moments undergo magnetic relaxation. Usually, the temperature at which M_{ZFC} shows a peak is taken as an average blocking temperature of the relaxing NPs. This parameter is higher in the powder than in the ferrofluid, which once again confirms that the magnetic relaxing behavior of the NPs is strongly affected by the dipolar interactions. The observation of magnetic irreversibility does not exclude the presence of NPs whose moments do not relax in the adopted experimental conditions and are in the blocked ferromagnetic state. This seems the case of the SD powder (Fig. 6d) where non-null H_C and M_r are measured even at T = 300 K (Fig. 4).

In the ferrofluids, H_C and M_r annihilate at T ~ 50 K. This is in favor of a superparamagnetic behavior of the NPs at higher temperature, but it is not conclusive.[27] Hence, to better ascertain the magnetic state of the NPs, we calculate a threshold size value D_{SP_1} above which the NPs of the ferrofluids are not superparamagnetic at T = 300 K. For this purpose, for each sample, we use the relation (2) to derive $D_{SP\_1} = V^{1/3}$, setting T_B = 300 K and K equal to K_{eff} (Table 2).[59] As already recalled, for SQUID measurements one considers t_m = 100 s, corresponding to a measurement frequency f_m = 0.01 Hz. The calculated D_{SP_1} values are reported in Table 2. Based on the size distributions obtained by TEM for the four samples (Fig. 2), we calculate that the fraction of NPs that are in the superparamagnetic

regime at T = 300 K is ~100% in SA and SB and SC and ~ 99% in SD. In short, practically all the NPs in the ferrofluids are superparamagnetic at T = 300 K, in the SQUID experimental conditions.

3.5 Magnetic heating properties

The heat released by magnetic NPs subjected to an alternating magnetic field, during one cycle, is equal to the area A of the resulting hysteresis loop. The SAR parameter, usually used to express the NPs heating efficiency, corresponds to the product between A and the frequency of the applied magnetic field. [16]

The magnetic heating properties of the Mn-doped magnetite NPs are tested by exposing, at room temperature (~ 300 K), 1 mL of ferrofluid to an alternating magnetic field for 900 seconds. The field amplitude is H_{max} = 228 Oe (i.e. 18 kA/m) and the frequency f_m = 245 kHz, corresponding to a measuring time $t_m = 1/f_m = 4 \times 10^{-6}$ s. These parameters respect the criterion to avoid detrimental effects on living organs, which recommends that ($H_{max} \times f_m$) does not exceed 5×10^9 A/m s. [60]

In Fig. 7a, for the four samples, typical curves of temperature increase $\Delta T(t)$ as a function of time t are plotted, being $\Delta T(t) = T(t) - T(t=0 \text{ s})$. The curves are well fitted by the Box-Lucas exponential function

$$\Delta T(t) = \Delta T_{max} \left(1 - e^{-\frac{t}{\tau}} \right) \tag{3}$$

in agreement with a model which assumes that the sample is in isoperibol conditions and that the losses between the sample and its environment are linear. In Equation (3), the fitting parameters are $\Delta T_{max} = T(t=900 \text{ s}) - T(t=0 \text{ s})$ and τ, i.e. the time needed to achieve a value of $\Delta T = 0.63 \Delta T_{max}$, usually indicated as the time constant of the heating process. The obtained values of ΔT_{max} and τ are indicated in Fig. 7a. ΔT_{max} increases from one sample to another, starting with SA and ending with SD, where it achieves the very remarkable value of ~ 76 °C.

The NPs that, in the adopted measurement conditions, are in the full superparamagnetic state are useless for generating heat because of their null hysteresis. Therefore, for each of the investigated samples, we calculate a new threshold size value D_{SP_2} above which the NPs of the ferrofluids are not superparamagnetic at T = 300 K. The calculation is similar to that done for D_{SP_1}, except for the value of the measuring time t_m. Hence, in relation (2), $\ln(t_m f_0) \sim 8$. Then, on the basis of the size distribution of each sample (Fig. 2), we estimate the fraction of NPs with size larger than D_{SP_2}, that is to say that they are in the blocked regime at T = 300 K. The obtained values and those of D_{SP_2} are reported in Table 2.

We estimate the parameter $\zeta = M_S V H_{max}/k_B T$, discriminating the regime of linear and non-linear response in a magnetic loop measurement. [16] In detail, for each sample, the minimum value of ζ, at T = 300 K, is calculated using the value of M_S in Table 1 and setting $V = (D_{SP\_2})^3$. In the four cases, $\zeta > 1$ (Table 2), namely we are not operating in the linear regime.

When the NPs are dispersed in a fluid, another magnetization mechanism may be active besides the internal rotation of the moments. This is the Brownian motion, namely the physical rotation of the NPs so that their moments align with the field. It is ruled by the relaxation time

$$\tau_B = 3\eta V_H/k_B T \qquad\qquad (4)$$

where η is the viscosity of the fluid (0.00542 P for octane) and V_H is the hydrodynamic volume of the suspended NPs.[20] Similarly to the Néel relaxation mechanism governed by τ_N, only the NPs for which $\tau_B > t_m$ ($f_m \tau_B > 1$) are thermally stable with regard to the Brown relaxation and generate heat, whereas those for which $\tau_B < t_m$ ($f_m \tau_B < 1$) do not. Hence, we put $\tau_B = t_m$ and we calculate a threshold value for the hydrodynamic size $D_B = (V_H)^{1/3}$ below which the NPs of the ferrofluids are thermally unstable, at T = 300 K. The value of D_B is the same for all the samples, ~ 22 nm.

Since, in each sample, $D_B > D_{SP\_2}$ (Table 2), the effective threshold parameter that determines the fraction of NPs that produce heat is D_B. However, the mean hydrodynamic size of the investigated NPs, estimated by DLS, is between 14 and 17 nm, similar for all the samples within an experimental error of 15% (Fig. S7). Therefore, the fraction of NPs with hydrodynamic size larger than D_B in each sample is expected to be vanishingly small or even null, which would mean that there are not NPs able to heat.

The only possibility is that the NPs with size $D > D_{SP\_2}$ have $\tau_N < \tau_B$ actually, so that D_{SP_2} is the effective threshold size and the heat is produced by the fractions of NPs, reported in Table 2, whose moments are blocked with regard to the relaxation mechanism of both Néel and Brown. This implies that the hydrodynamic volume in relation (4) does not correspond to that measured by DLS. We must conclude that, in a heating measurement, under the action of the alternating magnetic field and of the dipolar interactions, the NPs tend to form chains or agglomerates, [61, 62, 63] so that the resulting hydrodynamic volume satisfies the requirement that $\tau_N < \tau_B$ in all the NPs with $D > D_{SP\_2}$.

The whole description is supported by the result shown in Fig. 7b. The ΔT_{max} values are divided by the mass of the magnetic NPs in the ferrofluid (m_{magn}), obtained by subtracting from the whole mass of the sample the weight of the oleate (Table 1). The $\Delta T_{max}/m_{magn}$ parameter depends linearly on the

fraction of blocked NPs at T = 300 K, i.e. with D > D_{SP_2} (Table 2). This indicates that all the NPs that are in the blocked regime contribute, practically in the same way, to the magnetic hysteresis and hence are involved in the heating mechanism, in line with the fact that $\zeta > 1$ and therefore the LRT approach is not applicable.

It is worth remarking that experimentally it is impossible to disentangle the contributions to the magnetic hysteresis given by the reversal of the magnetic moments of the NPs and by the physical rotations of the NPs in the fluid in which they are dispersed.[16, 61] The matter could be possibly addressed using a theoretical approach, although the problem of calculating the hysteresis loss of a NP when both magnetization mechanisms are allowed appears very challenging.[64, 65]

One can object that for the calculation of D_{SP_1} and D_{SP_2}, in which we set $T_B = 300$ K, we use the values of K_{eff} at T = 5 K. Being K_{eff} determined by the dipolar interactions between the NPs, one may expect that K_{eff} decreases on rising temperature as an increasing fraction of NPs become superparamagnetic. Actually, the dipolar interactions play a role in determining the equilibrium state of the magnetic moments of the NPs also when they are in the superparamagnetic state, providing that the relaxation time characterizing the moment-moment interaction is smaller than the Néel relaxation time τ_N expressed by the relation (1). [66] Moreover, K_{eff} can be expected to reduce to a certain extent with increasing temperature because of the M_S decrease. However, we have just inferred that the NPs tend to form agglomerates in the fluid during the heating measurement. Hence, passing from T = 5 K, where the NPs are physically blocked in the frozen octane, to T = 300 K, the distance between the NPs may even reduce during the heating test, thus compensating, as far as the strength of the dipolar coupling is concerned, the mentioned detrimental effects. Indeed, it is practically impossible to evaluate K_{eff} of the NPs subjected to a heating test, hence to an alternating field, at T = 300 K. Therefore, we have considered the only values of K_{eff} that we can reliably estimate, namely those for T = 5 K.

Operatively, the SAR can be calculated from the heating measurements shown in Fig. 7a through the initial slope method, using the relation [35]

$$SAR = \frac{C}{m_{magn}} \cdot \frac{\Delta T}{\Delta t} \qquad (5)$$

where C is the heat capacity of the ferrofluid and ΔT is the temperature increment during the short time interval Δt in which heat losses are supposed negligible; m_{magn} is the mass of the magnetic NPs without oleate, as already stated above. For each sample, $\Delta T/\Delta t$ is calculated as the slope of the linear

curve fitting the heating curve for t in the 0 - 50 s interval. The heat capacity C has been taken equal to that of octane (for octane, the specific heat is 2228 J/ kg K and the density is 703 kg/m^3), supposing the heat capacity of the NPs negligible compared to that of the fluid. In Fig. 7c, the obtained SAR values are shown as a function of the fraction of blocked NPs at T = 300 K. Again we find a linear relationship, according to which the SAR is null for a fraction of blocked NPs smaller than ~ 5.6 %. Hence, this last value may be considered as the minimum amount of NPs needed to have a not negligible heating efficiency, in the described experimental conditions.

The fraction of blocked NPs, estimated for T = 300 K, is expected to reduce progressively during the heating measurement itself just because the temperature rises. The way in which this fraction decreases in each sample is calculated as a function of T in the 27 -127 °C range (i.e., 300 – 400 K). The results are shown in Fig. 7d. In the same figure, the circular symbols correspond to the fraction of blocked NPs existing in each sample at the temperature reached after t = 900 s in the heating tests of Fig 7a. In other words, that is the amount of NPs that, after 900 s, are still able to generate enough heat to compensate for the losses with the environment, mechanism that determines the saturating trend of the heating curves in Fig. 7a.

Differently from theoretical predictions concerning the case of heating measurements performed in the regime of linear magnetic response [20], it follows that an assembly of highly monodispersed NPs with size close to D_{SP_2} is not especially suitable for magnetic heating applications since they can become superparamagnetic during the heating treatment, as soon as the temperature is raised above their T_B, due to the heat generated by themselves. To avoid this event one may conclude that the best solution is to employ NPs with a size large enough to be surely blocked, even at high temperatures.

However, the larger the NPs the less they can be described as macrospins, i.e. as canonical single magnetic domains, whose atomic spins reverse coherently. In fact, especially if the intrinsic anisotropy of the NPs is low, when the size is larger than 15-20 nm closure magnetization configurations, i.e. vortex-type, and incoherent reversal modes may become energetically favored, resulting in a lower coercivity and hence narrower hysteresis loops. [18, 19, 67]

Moreover, large NPs are more difficult to stabilize in a colloidal suspension and, above all, to be useful for biological applications, the size of the NPs must not exceed a few tens of nanometers, depending on the specific use, to allow the interaction with cells. [68]

In the case of the presented experimental study, we expect that the heating capacity would be further improved if we were able to prepare NPs with a size distribution similar to that of sample SD, but slightly shifted to the right, so as to increase the fraction of blocked NPs, preserving the macrospin description. We have tried to reach this goal by increasing t300 up to 240 minutes, but the results

have not been satisfactory. In fact, any reaction performed for a reflux time longer than 180 minutes led to NPs very similar to SD, therefore not succeeding in substantially modifying the size distribution and therefore the magnetic properties. This observation suggests that after t300 = 180 minutes the thermal decomposition of the organometallic precursors is substantially completed, leading to the formation of either the desired NPs or of inactive metal-based byproducts.

Finally, heating measurements are performed on sample SD under different alternating fields. In particular, the frequency is f_m = 245 kHz (as before) and H_{max} = 57, 113, 170 and 228 Oe. The SAR values are calculated using relation (5) and the results are shown as a function of the parameter ζ in Fig. 8. Obviously, the hysteresis loop area of a magnetic system increases with increasing the amplitude of the applied field. Accordingly, the SAR is expected to rise with increasing ζ, as indeed observed. However, an abrupt change of the SAR parameter is observed around ζ = 1, confirming that this last condition marks a change of regime in the magnetic heating mechanism.

This result also indicates that increasing the field frequency f_m is not a good solution in order to rise the fraction of blocked NPs. In fact, even doubling the value of f_m (not feasible with our experimental apparatus) results in a reduction of D_{SP_2} less than 2%, which does not affect the calculated amount of blocked NPs. Performing hyperthermia treatments on living beings at such a high f_m may be risky. To comply with the safety criterion previously indicated, it is advisable to halve H_{max} and hence ζ. As shown in Fig. 8, this would be definitely detrimental to the heating efficiency.

Conclusions

We have studied the structural, compositional and magnetic properties of a set of samples of Mn-doped magnetite NPs and elucidated their strict connection with the mechanism underlying the magnetic heating effect.

By varying the parameter t300, i.e. the duration of the reflux treatment at 300 °C during the synthetic procedure, we have succeeded in changing the size distribution of the NPs. Thanks to the Mn doping, we have prepared NPs with high M_S values, compared to NPs of pure magnetite. Although the Mn/Fe atomic ratio is the same in all the samples ($\sim$ 0.18 on average, as estimated by ICP-MS), M_S increases on increasing t300 (a value as high as $\sim$ 94 emu/g is measured in the SD NPs, at T = 5 K). We have related this effect to the concomitant increase of the mean size D_{ave} and to a different distribution of the Mn^{2+} ions in the B sites of the spinel structure, in line with the observed reduction of the Néel temperature T_N.

The M_S enhancement and the evolution of the size distribution lead to an increase in the strength of dipolar magnetic interactions between the NPs and we have shown that this results in an effective magnetic anisotropy also varying from sample to sample depending on t300. In turn, for a fixed frequency of the external alternating field applied in a heating measurement, the effective anisotropy determines the fraction of NPs that are in the superparamagnetic regime. Moreover, the value of M_S and the size of the NPs together with the amplitude of the alternating field characterize the magnetic behaviour of the NPs assembly in terms of linear or non-linear response, depending on the value of the ζ parameter.

Indeed, the structural and magnetic properties of the samples and the parameters of the external magnetic field are very closely intertwined. However, we have shown that, for a field with amplitude and frequency suitable for biomedical applications (228 Oe and 245 kHz respectively, at which $\zeta > 1$ in all the samples), this complex interplay results in a simple heating mechanism, apparently at least. In fact, the SAR depends linearly on the fraction of NPs, that we have calculated, which, at T = 300 K, are thermally stable regarding the Néel relaxation and, as we have discussed, also regarding the Brown relaxation. This finding implies that, in the adopted experimental conditions, all the NPs that are in the blocked regime – small enough to be modeled as macrospins - contribute equally to the heat generation.

In the sample SD the interplay between the intrinsic physical properties of the NPs and the measurement parameters is highly virtuous and remarkable heating performances are observed. In particular, at the above indicated field, the SAR ~ 73 W/g and a temperature increase $\Delta T \sim 48$ °C is obtained in $\tau = 153$ s, time constant of the heating process. This good heating capacity coupled to the small mean size, which does not exceed 10 nm, make the SD NPs especially promising as hyperthermia agents in biomedical applications.

Beyond this satisfactory result, the noteworthy point is the possibility of adjusting the heating capacity of the produced NPs, so as to match specific needs, changing only a single synthesis parameter. By acting on t300, we can control M_S and the NPs size distribution to a good extent, and hence, through the key intervention of the dipolar interactions, modulate the heating efficiency.

Conflicts of interest

There are no conflicts to declare

Table 1. The data are relative to the samples labelled as indicated in Column 1. Column 2: mean size of the NPs D_{ave}, estimated by TEM. Column 3: weight fraction of the oleate as estimated by TGA measurements. Columns 4 and 5: saturation magnetization M_S at $T = 5$ K and 300 K, respectively.

Sample	Mean Size D_{ave} (nm) $\pm 5\%$	Oleate wt. fraction (%) ± 1	M_S at T = 5 K (emu/g) $\pm 2\%$	M_S at T = 300 K (emu/g) $\pm 2\%$

SA	6.8	24	79.7	63.4
SB	8.1	18	85.1	70.1
SC	8.4	15	86.7	70.3
SD	9.5	15	94.0	77.5
SRef	8.8	19	73.1	62.9

Table 2. The data are relative to the samples labelled as indicated in Column 1. Columns 2 and 3: irreversibility field H_{irr} at $T = 5$ K for the samples in form of powder and effective magnetic anisotropy K_{eff}. Columns 4 and 5: irreversibility field H_{irr} at $T = 5$ K for the samples in form of ferrofluid and effective magnetic anisotropy K_{eff}. Columns 7 and 8: threshold size values related to the Néel relaxation of the NPs in form of ferrofluid, calculated for $f_m = 0.01$ Hz and $f_m = 245$ kHz respectively, for $T_B = 300$ K. Column 9: fraction of blocked NPs at $T = 300$ K. Column 10: parameter ζ at $T = 300$ K for $H_{max} = 228$ Oe.

Sample	H_{irr} (Oe) ± 2% Powder	K_{eff} (10^5erg/cm^3) ± 3% Powder	H_{irr} (Oe) ± 2% Ferrofluid	K_{eff} (10^5 erg/cm^3) ± 3% Ferrofluid	D_{SP_1} (nm) T_B = 300 K f_m = 0.01 Hz ± 2% Ferrofluid	D_{SP_2} (nm) T_B = 300 K f_m = 245 kHz ± 2% Ferrofluid	Blocked NPs at T = 300 K (%) Ferrofluid	ζ T = 300 K
SA	1250	2.5	1090	2.2	16.8	11.5	6.5 ± 1.0	~2.7
SB	1520	3.3	1090	2.4	16.3	11.1	9.8 ± 1.2	~2.7
SC	1730	3.9	1200	2.7	15.6	10.7	14.6 ± 1.4	~2.4
SD	2210	5.3	1250	3.0	15.1	10.3	24 ± 2	~2.4
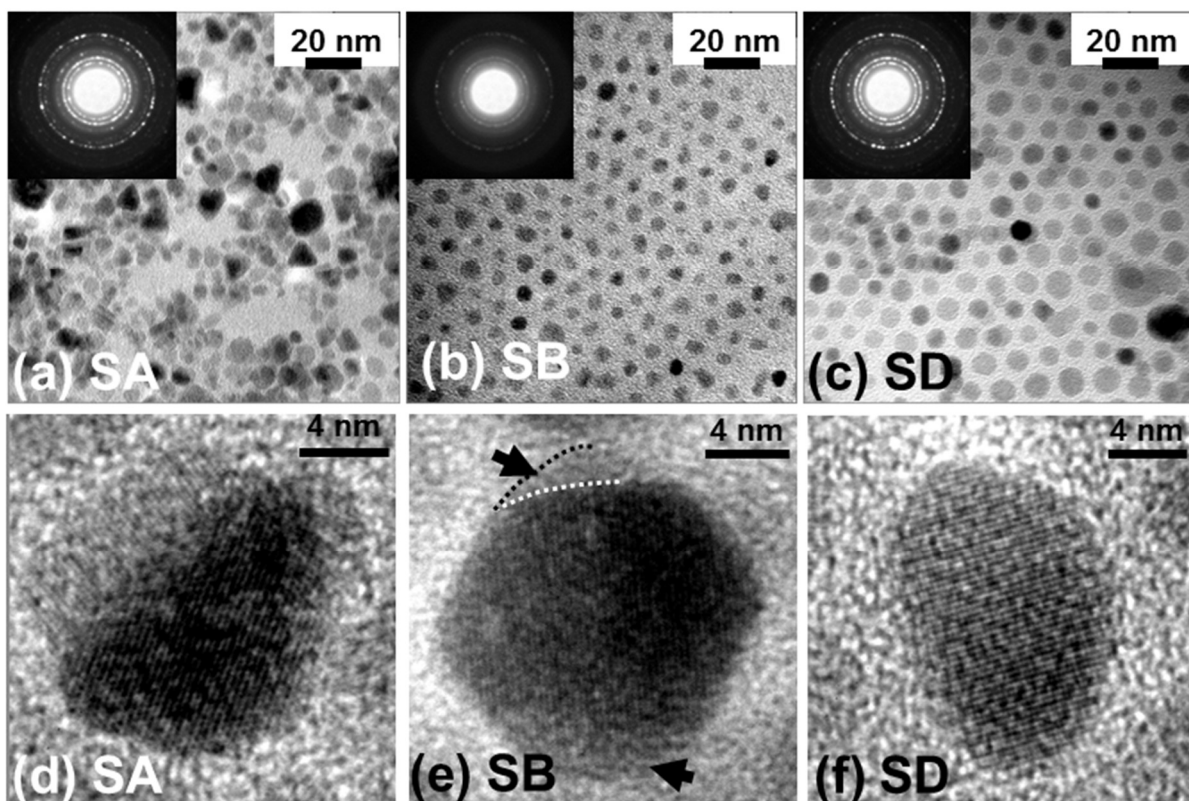
Figure 1. TEM images and SAED patterns (up-left insets) for the samples SA (a), SB (b) and SD (c). HR-TEM images for SA (d), SB (e) and SD (f). In frame (e), the arrows point at nearly amorphous regions of the displayed NP (see text for details).
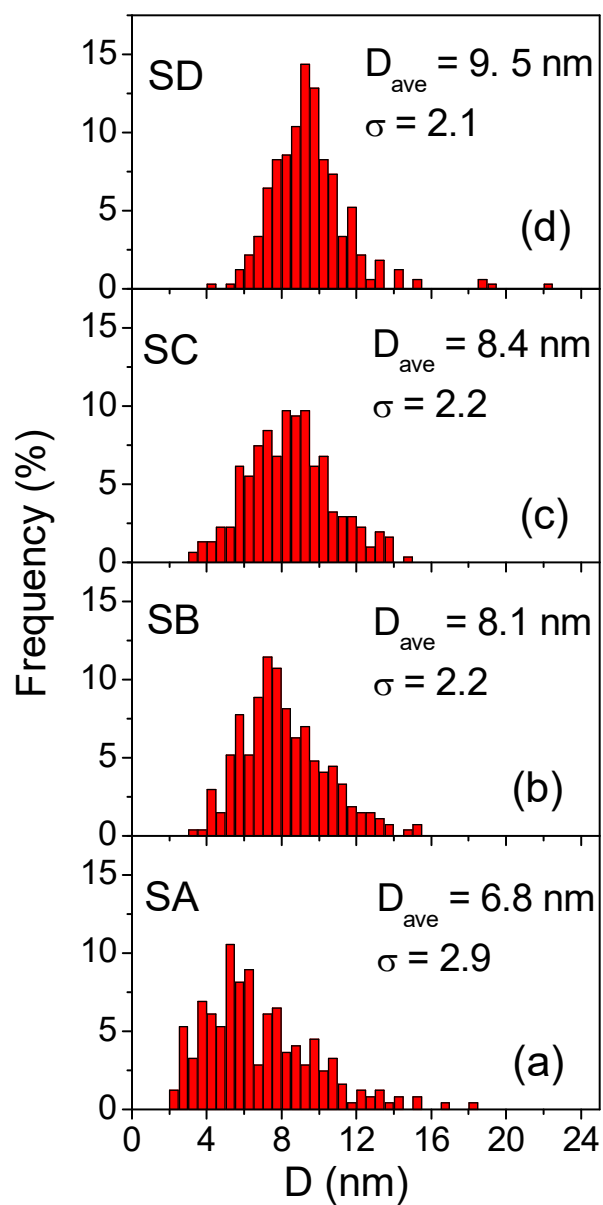
Figure 2. Size distributions of the Mn-doped magnetite NPs, estimated by TEM. The results for the four investigated samples (SA, SB, SC and SD) are shown together with the values of the mean size D_{ave} and of the standard deviation σ.
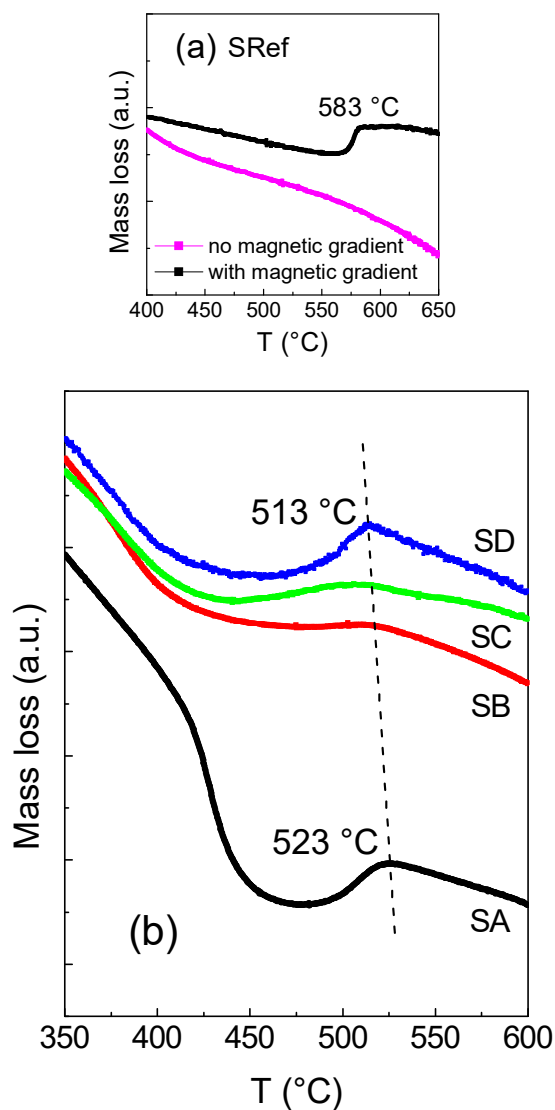
Figure 3. (a) Mass loss vs. temperature (T) measured on the reference sample of magnetite NPs (SRef) with (upper curve) and without (lower curve) magnetic field gradient. The measurement in gradient allows the Néel temperature T_N to be estimated. (b) Mass loss vs. T measured in the samples of Mn-doped magnetite NPs with magnetic field gradient. The dotted line is a guide to the eye that intercepts the different curves at T_N (the values of T_N for samples SA and SD are reported).
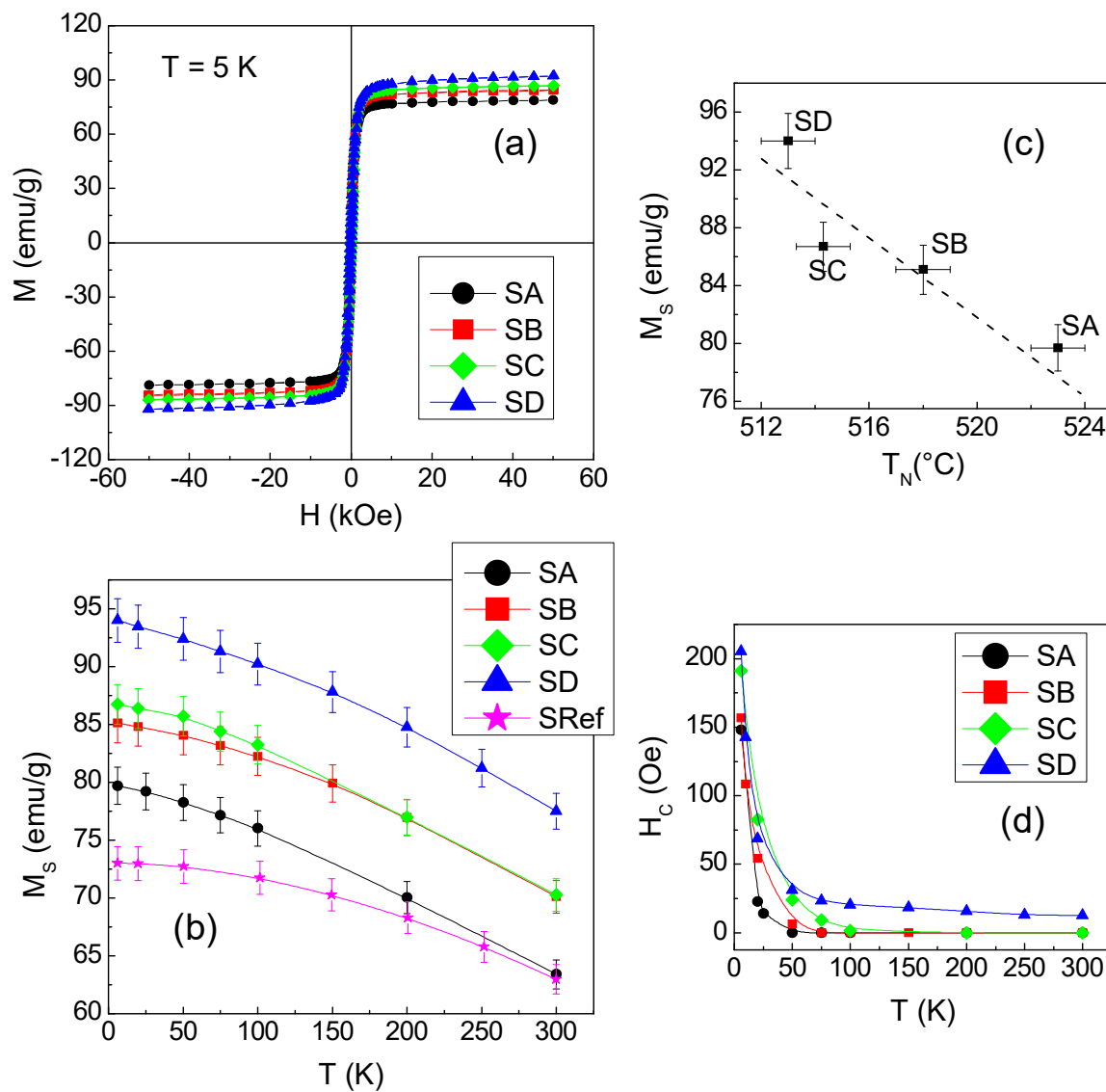
Figure 4. (a) Magnetic hysteresis loops measured on the Mn-doped magnetite NPs in form of powder, at T = 5 K. (b) Saturation magnetization (M_S) vs. T for the Mn-doped magnetite NPs and for magnetite NPs taken as reference sample (SRef). (c) M_S, measured at T = 5 K on the Mn-doped magnetite NPs, vs. the Néel temperature T_N estimated by TGA (the dotted line is a guide to the eye). (d) Coercivity (H_C) vs. T for the samples of Mn-doped magnetite NPs (the error bars are smaller than the symbol size).
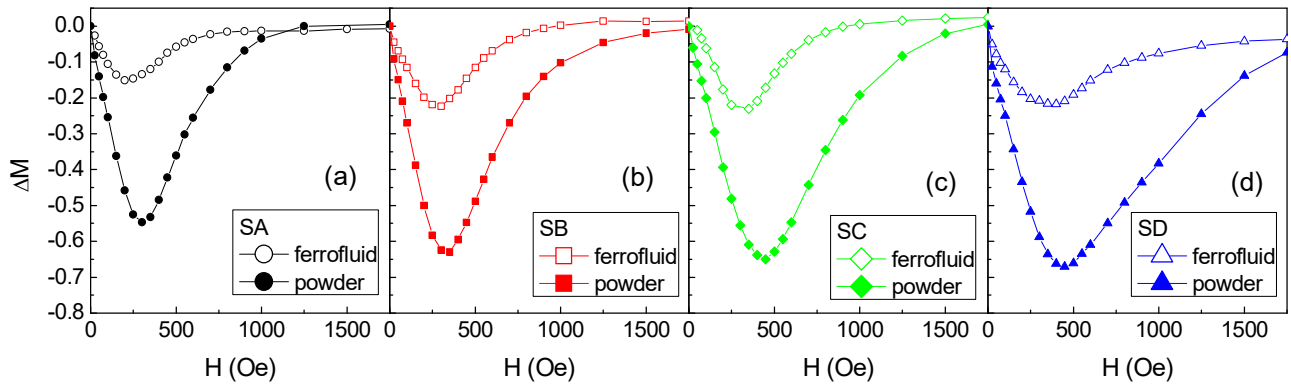
Figure 5. ΔM-plots measured at T = 5 K on the Mn-doped magnetite NPs in form of ferrofluid (open symbols) and of powder (full symbols).
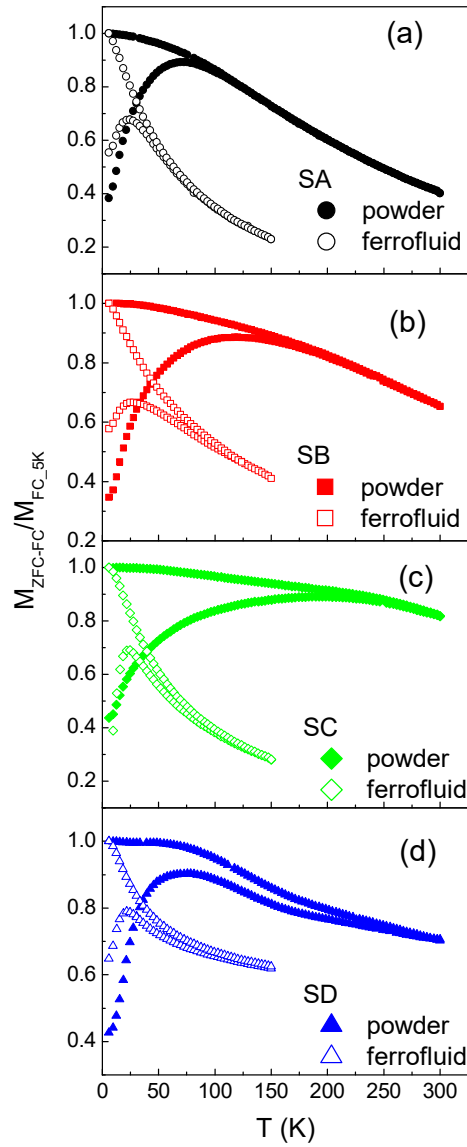
Figure 6. Magnetization measured on the Mn-doped magnetite NPs in form of powder (full symbols) and of ferrofluid (open symbols) for increasing temperature at $H_{appl} = 20$ Oe, after zero-field-cooling (M_{ZFC}, lower branch of each displayed curve) and after field-cooling (M_{FC}, upper branch). The curves are normalized to the value of M_{FC} at $T = 5$ K.
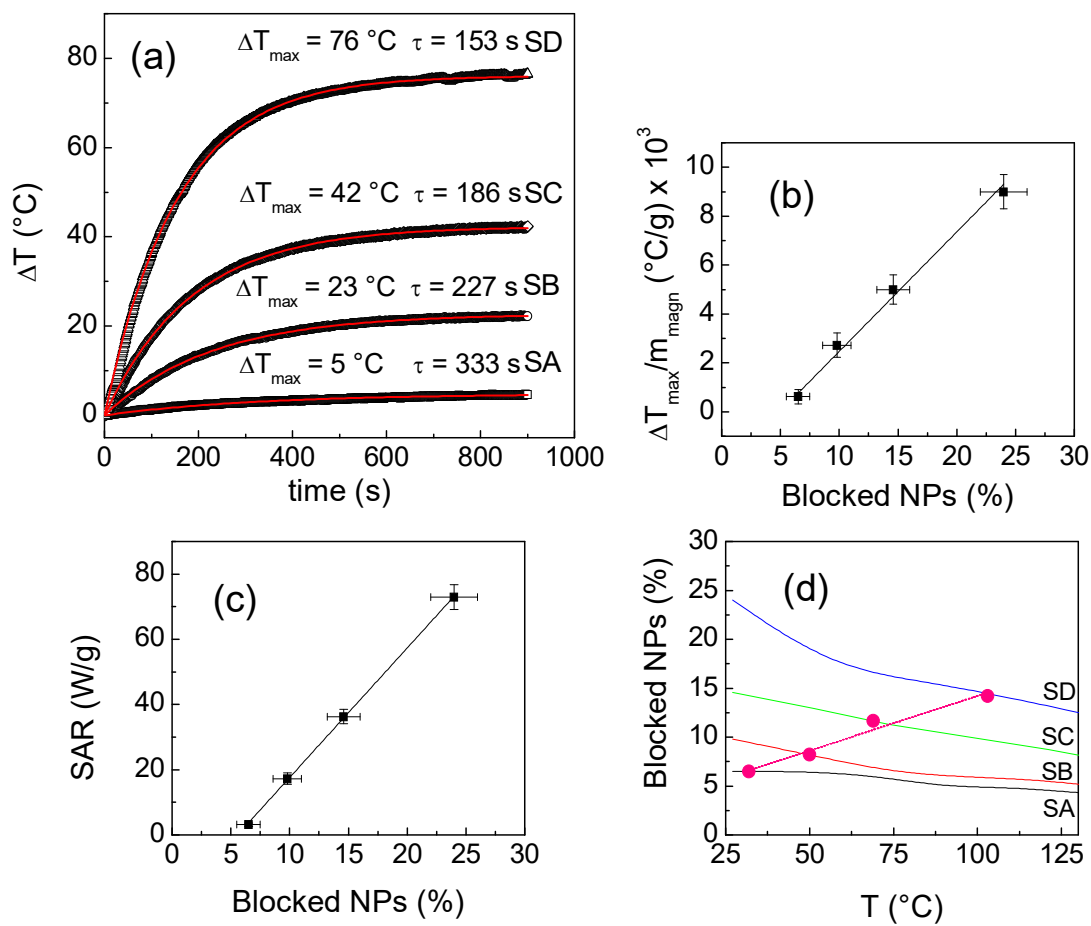
Figure 7. (a) Heating curves for the Mn-doped magnetite NPs in form of ferrofluids, subjected to an alternating magnetic field of amplitude H_{max} = 228 Oe and frequency f_m = 245 kHz. The curves of temperature increase ΔT vs. time are shown (black symbols). The continuous red lines are the fitting curves by the Box-Lucas exponential function; the calculated values of ΔT_{max} and of the time constant of the heating process τ are reported (see text for details). (b) Values of ΔT_{max}, normalized to the mass of the NPs in the ferrofluids (m_{magn}), shown as a function of the fraction of blocked NPs in each sample; the continuous line is the linear fit of the data. (c) SAR values, calculated from the heating curves in frame (a), vs. the fraction of blocked NPs in each sample; the continuous line is the linear fit of the data. (d) Thermal dependence of the fraction of blocked NPs in each sample, calculated for the 27 – 127 °C temperature range (i.e., 300 – 400 K). The full circular symbols correspond to the fraction of blocked NPs existing at the temperature reached after 900 s in the heating measurements shown in frame (a) (the dotted line is a guide to the eye).
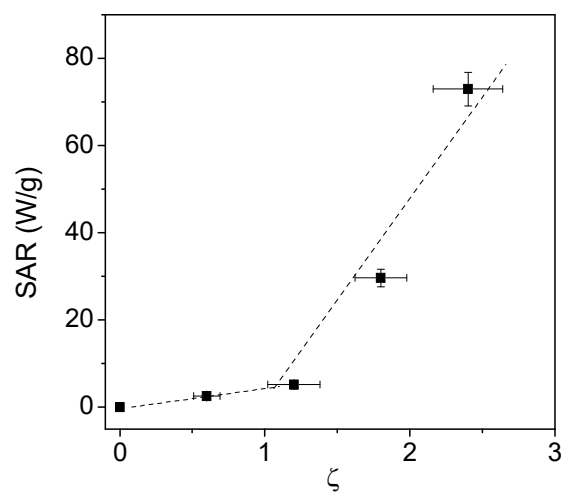
Figure 8. SAR measured on the ferrofluid SD at different amplitudes of the alternating magnetic field (frequency $f_m = 245$ kHz), corresponding to different values of the parameter ζ (the dotted lines are guides to the eye). See text for explanation.

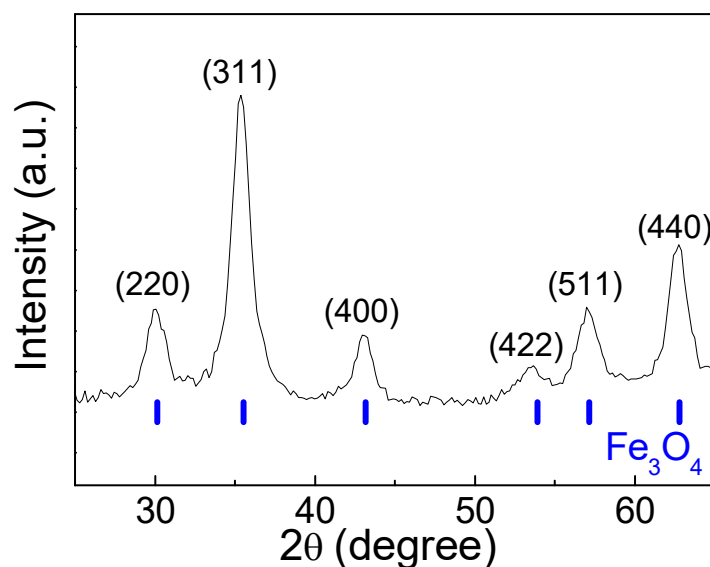**Electronic Supplementary Information (ESI)**

X-ray Diffraction (XRD)

Figure S1. XRD spectrum of sample SD, collected using a PANalytical θ/θ diffractometer (CuKα radiation; 40 kV and 40 mA). Broad peaks are visible corresponding to the spinel structure of magnetite (

Energy dispersive X-ray spectrometry (EDS)

Energy dispersive X-ray spectrometry (EDS) measurements are performed on the SA, SB, SC and SD samples in a Philips XL20 scanning electron microscope (SEM) equipped with a microanalysis system EDAX Phoenix (detector ECON IV). The analysis is performed on the same samples investigated by TEM, namely the TEM grids containing the NPs are mechanically attached to a home-made stub suitable to be introduced in a SEM.

A typical EDS spectrum (in particular, for sample SD), is shown in Fig. S2. The Mn and Fe signals are clearly visible and the areas under the peaks allow the software (ZAF correction) to calculate the ratio of their atomic concentration in the sample.

The atomic ratio Mn/Fe is equal to (0.22 ± 0.06) in SD and is similar in all the samples within the errors, in good agreement with the ICP-MS results reported in the main text. The Cu signal comes from the TEM grid used to collect the NPs (the C peak, due to the carbon film on the copper grid, is observed at lower energy and therefore it does not appear in the figure).
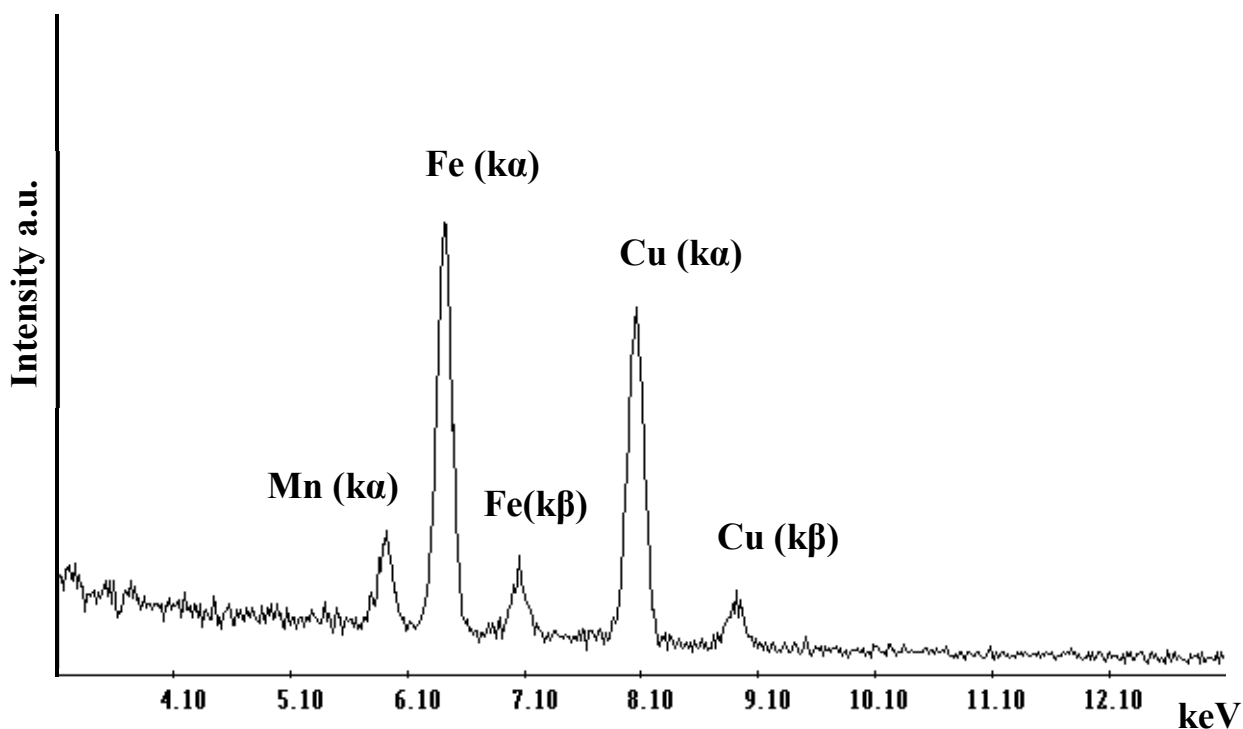
Figure S2. EDS spectrum of sample SD

Fourier transform infrared spectroscopy (FT-IR)

The transmission IR spectra of the NPs samples in KBr pellets are recorded on a Perkin-Elmer Spectrum 100 FT-IR spectrophotometer in the region 250-4000 cm^{-1}. They appear similar for all the samples. As an example, the spectrum of sample SA is reported in Fig. S3. The bands at 1410 cm^{-1}, 1543 cm^{-1}, 2850-2920 cm^{-1} and 3370 cm^{-1} are related to the oleate; the bands at 392 and 573 cm^{-1} are due to the iron-oxide phase.
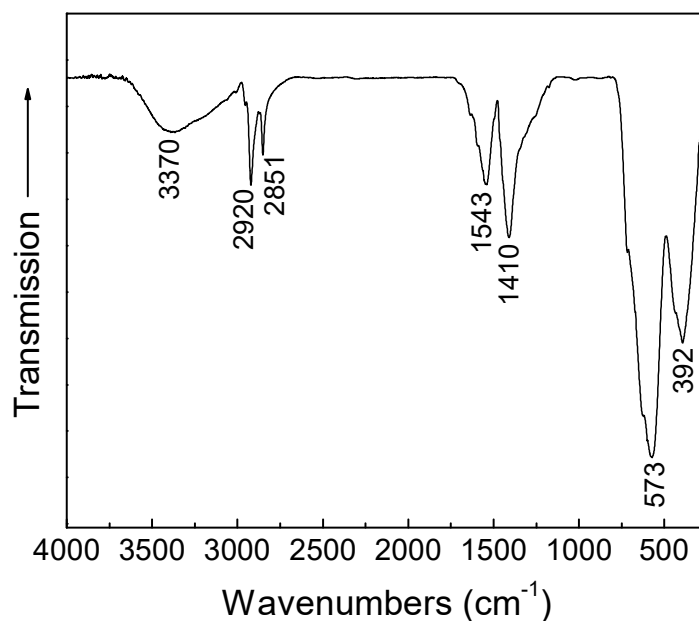

Figure S3. FT-IR spectrum of sample SA.

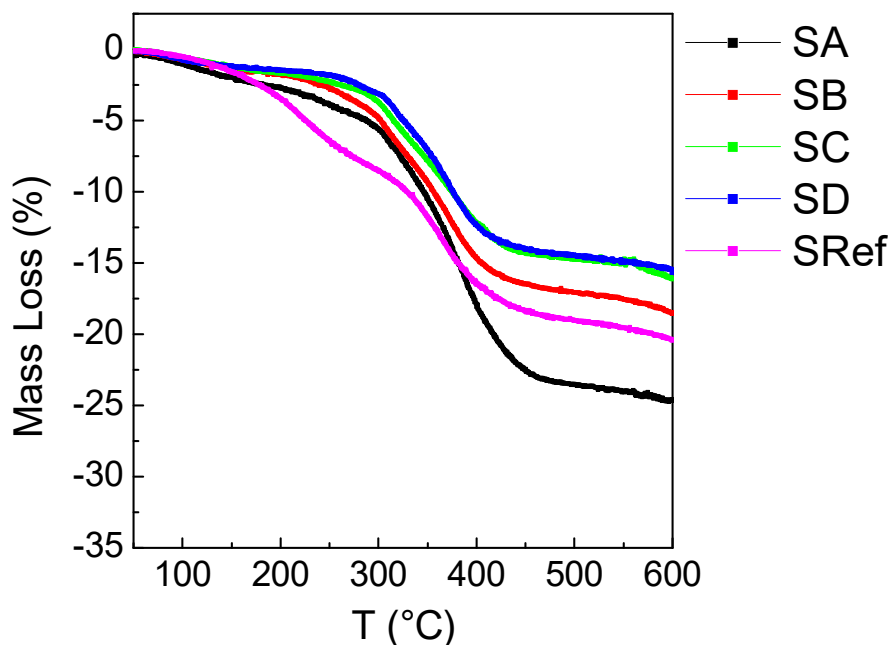## Thermogravimetric analysis (TGA)

Figure S4. Mass loss vs. T measured in the samples of Mn-doped magnetite NPs and on the reference magnetite NPs (SRef), allowing the weight fraction of oleate in the samples to be estimated.

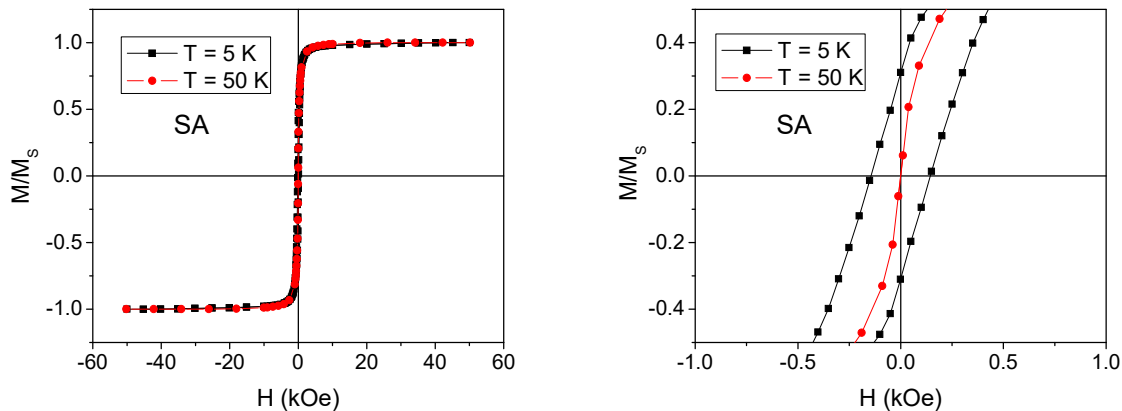## SQUID measurements on samples in form of ferrofluid

Figure S5. Left: magnetic hysteresis loops measured on sample SA in form of ferrofluid at T = 5 K and 50 K (normalized to the saturation magnetization M_S). Right: enlarged view of the central region of the loops.
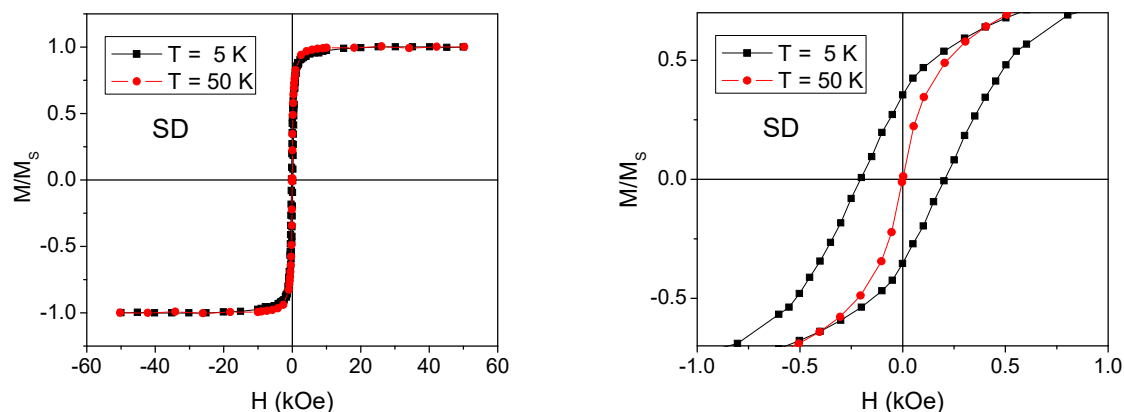
Figure S6. Left: magnetic hysteresis loops measured on sample SD in form of ferrofluid at T = 5 K and 50 K (normalized to the saturation magnetization M_S). Right: enlarged view of the central region of the loops.

Figs. S5 and S6 show the hysteresis loops measured on ferrofluids SA and SD, respectively. In both cases, the coercivity H_C and the remanent magnetization M_r are null at T = 50 K. The same behavior is observed in the ferrofluids SB and SC.

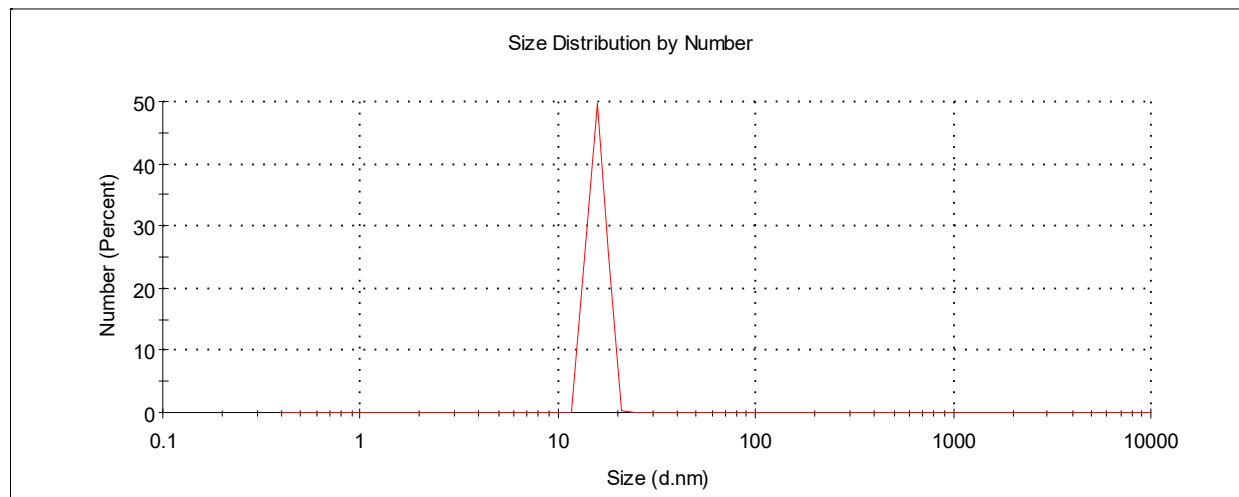## Dynamic Light Scattering analysis (DLS) analysis

Figure S7. Hydrodynamic size distribution of the SB NPs measured by DLS in n-octane. The mean hydrodynamic diameter is (15 ± 2) nm. Similar results are obtained for the other samples of Mn-doped magnetite NPs. In fact, the measured values of the mean hydrodynamic size are between 14 and 17 nm, similar for all the samples within the experimental error of 15%. These values are consistent with what is expected for oleate-coated NPs with physical size of the order of 10 nm, as in our case, dispersed in an apolar solvent [F. Arteaga-Cardona et al., *J. All. Comp.,* 2016, **663**, 636; P. de la Presa et al., *J. Phys. Chem. C*, 2015, *119*, 11022].

References

[1] Q. A. Pankhurst, N.K.T. Thanh, S.K. Jones and J. Dobson, *J. Phys. D: Appl. Phys.*, 2009, **42**, 224001. DOI: 10.1088/0022-3727/42/22/224001

[2] T.D. Schladt, K. Schneider, H. Schild and W. Tremel, *Dalton Trans.*, 2011, **40**, 6315. DOI: 10.1039/c0dt00689k

[3] W. Wu, C. Zhong Jiang and V.A. L. Roy, *Nanoscale*, 2016, **8**, 1942. DOI: 10.1039/C6NR07542H

[4] L.M. Bauer, S.F. Situ, M.A. Griswold and A.C.S. Samia, *Nanoscale*, 2016, **8**, 12162. DOI: 10.1039/C6NR01877G

[5] E. A. Périgo, G. Hemery, O. Sandre, D. Ortega, E. Garaio, F. Plazaola, and F. J. Teran, *Appl. Phys.Rev.*, 2015, **2**, 041302. DOI: 10.1063/1.4935688

[6] S. Tong, C.A. Quinto, L. Zhang, P. Mohindra and G. Bao, *ACS Nano*, 2017, **11**, 6808. DOI: 10.1021/acsnano.7b01762

[7] P. Guardia, R. Di Corato, L. Lartigue, C. Wilhelm, A. Espinosa, M. Garcia-Hernandez, F. Gazeau, L. Manna and T. Pellegrino, *ACS Nano,* 2012, **6**, 4, 3080. DOI: 10.1021/nn2048137

[8] J.H. Lee, J.T. Jang, J.S. Choi, S.H. Moon, S.H. Noh, J.W. Kim, J.G. Kim, I.S. Kim, K.I. Park and J. Cheon, *Nat Nanotechnol.*, 2011, **6**, 418. DOI: 10.1038/nnano.2011.95

[9] C. Blanco-Andujar, D. Ortega, P. Southern, Q. A. Pankhurst and N. T. K. Thanh, *Nanoscale*, 2015, **7**, 1768. DOI: 10.1039/C4NR06239F

[10] R. Ivkov, S.J. DeNardo, W. Daum, A. R. Foreman, R.C. Goldstein, V. S. Nemkov and G.L. DeNardo, *Clin Cancer Res,* 2005, **11**, 7093s. DOI: 10.1158/1078-0432.CCR-1004-0016

[11] A. Hervault and Nguyễn Thị Kim Thanh, *Nanoscale*, 2014, **6**, 11553. DOI: 10.1039/C4NR03482A

[12] S. Moise, J. M. Byrne, A. J. El Haj and N. D. Telling, *Nanoscale*, 2018,**10**, 20519. DOI: 10.1039/C8NR05946B

[13] U. M. Engelmann, A.A. Roeth, D. Eberbeck, E.M. Buhl, U.P. Neumann, T.Schmitz-Rode and I. Slabu, *Scientific Reports,* 2018*,* **8**, 13210. DOI: 10.1038/s41598-018-31553-9

[14] C. S. S. R. Kumar and F. Mohammad, *Advanced Drug Delivery Reviews,* 2011*,* **63,** 789. DOI:10.1016/j.addr.2011.03.008

[15] L. de Alcântara Sica de Toledo, H. Cássia Rosseto, R. Said dos Santos, F. Spizzo, L. Del Bianco, M. Camotti Montanha, E. Esposito, E. Kimura, P. S. Bonfim-Mendonça, T. Inez Estivalet Svidzinski, R. Cortesi and M. Luciano Bruschi, *AAPS PharmSciTech,* 2018, **19**, 3258. DOI: 10.1208/s12249-018-1163-4

[16] J. Carrey, B. Mehdaoui, and M. Respaud, *J. Appl. Phys.*, 2011, **109**, 083921. DOI: 10.1063/1.3551582

[17] B.D. Cullity and C.D. Graham, *Introduction to Magnetism and Magnetic Materials*, Wiley-IEEE Press, Piscataway NJ, USA, 2nd ed, 2009.

[18] A. Hubert and R. Schäfer, *Magnetic Domains,* Springer, Berlin, 1998.

[19] J.M.D. Coey, *Magnetism and Magnetic Materials*, Cambridge University Press, Cambridge, 2010.

[20] R.E. Rosensweig, *J. Magn. Magn. Mater.*, 2002, **252**, 370.
DOI: 10.1016/S0304-8853(02)00706-0

[21] J.L. Dormann, D. Fiorani and E. Tronc, *Adv. Chem. Phys.*, 1997, **XCVIII**, 283.
DOI:10.1002/9780470141571.ch4

[22] M. Blanco-Mantecon and K. O'Grady, *J. Magn. Magn. Mater.*, 2006, **296**, 124. DOI: 10.1016/j.jmmm.2004.11.580

[23] J.M.D. Coey, *Phys. Rev. Lett.*, 1971, **27**, 1140. DOI:10.1103/PhysRevLett.27.1140.

[24] F.T. Parker, M.W. Foster, D.T. Margulies and A.E. Berkowitz, *Phys. Rev. B*, 1993, **47**, 7885. DOI:10.1103/PhysRevB.47.7885

[25] M.P. Morales, C.J. Serna, F. Bødker and S. Mørup, *J. Phys.: Condens. Matter*, 1997, **9**, 5461. DOI:10.1088/0953-8984/9/25/013.

[26] F. Spizzo, P. Sgarbossa, E. Sieni, A. Semenzato, F. Dughiero, M. Forzan, R. Bertani and L. Del Bianco, *Nanomaterials,* 2017, **7***,* 373. DOI:10.3390/nano7110373

[27] L. Del Bianco, I.G. Lesci, G. Fracasso, G. Barucca, F. Spizzo, M. Tamisari, R. Scotti and L. Ciocca, *Mater. Res. Express*, 2015, **2**, 065002. DOI: 10.1088/2053-1591/2/6/065002

[28] J. Giri, P. Pradhan, T. Sriharsha and D. Bahadur, *J. Appl. Phys.*, 2005, **97**, 10Q916. DOI: 10.1063/1.1855131

[29] J. Jang, H. Nah, J.H. Lee, S. H. Moon, M. G. Kim and J. Cheon, *Angew. Chem. Int.*, 2009, **48**, 1234. DOI: 10.1002/anie.200805149

[30] R. Otero-Lorenzo, E. Fantechi, C. Sangregorio and V. Salgueiriño, *Chem. Eur. J.*, 2016, **22**, 6666. DOI : 10.1002/chem.201505049

[31] M.F. Casula, E. Conca, I. Bakaimi, A. Sathya, M. E. Materia, A. Casu, A. Falqui, E. Sogne, T. Pellegrino and A.G. Kanaras, *Phys. Chem. Chem. Phys.,* 2016*,* **18**, 16848.
DOI: 10.1039/C6CP02094A

[32] L. Yang, L. Ma, J. Xin, A. Li, C. Sun, R. Wei, B.W. Ren, Z. Chen, H. Lin and Jinhao Gao, *Chem. Mater.*, 2017, **29**, 3038. DOI: 10.1021/acs.chemmater.7b00035

[33] M.S.A. Darwish, *Journal of Molecular Liquids*, 2017, **231**, 80.
DOI: 10.1016/j.molliq.2017.01.094

[34] M. Coïsson, G. Barrera, F. Celegato, L. Martino, S. N. Kane, S. Raghuvanshi, F. Vinai and P. Tiberto, *Biochimica et Biophysica Acta*, 2017, **1861**, 1545. DOI: 10.1016/j.bbagen.2016.12.006

[35] I. Andreu and E. Natividad, *Int J Hyperthermia*., 2013 **29**, 739. DOI: 10.3109/02656736.2013.826825.

[36] S. Sun, H. Zeng, D.B. Robinson, S. Raoux, P.M. Rice, S.X. Wang and G. Li, *J. Am. Chem. Soc.*, 2003, **126**, 273. DOI: 10.1021/ja0380852

[37] M. Coïsson, G. Barrera, C. Appino, F. Celegato, L. Martino, A.P. Safronov, G.V. Kurlyandskaya and P. Tiberto, *J. Magn. Magn. Mater.*, 2019, **473**, 403. DOI:10.1016/j.jmmm.2018.10.107

[38] U.M. Engelmann, C. Shasha, E. Teeman, I. Slabu, K.M. Krishnan, *J. Magn. Magn. Mater.*, 2019, **471**, 450. DOI:10.1016/j.jmmm.2018.09.041

[39] F. Arteaga-Cardona, K. Rojas-Rojas, R. Costo, M.A. Mendez-Rojas, A. Hernando and P. de la Presa, *J. All. Comp.,* 2016, **663**, 636. DOI:10.1016/j.jallcom.2015.10.285.

[40] A. Jordan, R. Scholz, K. Maier-Hauff, M. Johannsen, P. Wust, J. Nadobny, H. Schirra, H. Schmidt, S. Deger, S. Loening, W. Lanksch and R. Felix, *J. Magn. Magn. Mater.*, 2001, **225**, 118. DOI: 10.1016/S0304-8853(00)01239-7

[41] P. Di Barba, F. Dughiero and E. Sieni, *IEEE Trans. Magn.*, 2010, **46**, 2931. DOI:10.1109/TMAG.2010.2044769.

[42] M. Iwahashi, Y. Kasahara, H. Matsuzawa, K. Yagi, K. Nomura, H. Terauchi, Y. Ozaki and M. Suzuki, *J. Phys. Chem*. B, 2000, **104**, 6186. DOI: 10.1021/jp000610l

[43] G. Salas, C. Casado, F. J. Teran, R. Miranda, C. J. Serna and M. Puerto Morales, *J. Mater. Chem.*, 2012, **22**, 21065. DOI: 10.1039/c2jm34402e

[44] http://www.gatan.com/products/tem-analysis/gatan-microscopy-suite-software accessed February 2019)

[45] Q. Song, Y. Ding, Z. Lin Wang and Z. John Zhang, *Chem. Mater.*, 2007, **19**, 4633. DOI: 10.1021/cm070990o

[46] L. Zhang, R. He and H.C. Gu, Applied Surface Science, 2006, 253, 2611. DOI: 10.1016/j.apsusc.2006.05.023

[47] A.G. Roca , M. P. Morales, K. O'Grady and C. J. Serna, *Nanotechnology*, 2006, **17**, 2783. DOI: 10.1088/0957-4484/17/11/010

[48] D. Carta, M. F. Casula, P. Floris, A. Falqui, G. Mountjoy, A. Boni, C. Sangregorio and A. Corrias, *Phys. Chem. Chem. Phys*., 2010, **12**, 5074. DOI: 10.1039/b922646j

[49] Aria Yang, C. N. Chinnasamy, J. M. Greneche, Yajie Chen, Soack D. Yoon, Kailin Hsu, C. Vittoria and V. G. Harris, *Appl. Phys. Lett.*, 2009, **94**, 113109. DOI: 10.1063/1.3099340

[50] C. Binns, M.J. Maher, Q.A. Pankhurst, D. Kechrakos and K.N. Trohidou, *Phys. Rev. B*, 2002, **66**, 184413. DOI: 10.1103/PhysRevB.66.184413

[51] P. Allia, M. Coisson, P. Tiberto, F. Vinai, M. Knobel, M.A. Novak and W.C. Nunes, *Phys. Rev. B*, 2001, **64**, 144420. DOI: 10.1103/PhysRevB.64.144420

[52] L. Del Bianco, D. Fiorani, A.M. Testa, E. Bonetti, L. Savini and S. Signoretti, *Phys. Rev. B*, 2002, **66**, 174418-1. DOI:10.1103/PhysRevB.66.174418.

[53] P.E. Kelly, K. O'Grady, P.I. Mayo and R.W. Chantrell, *IEEE Trans. Magn.*, 1989, **25,** 3881. DOI: 10.1109/20.42466

[54] J. Garca-Otero, M. Porto and J. Rivas, *J. Appl. Phys.*, 2000, **87**, 7376. DOI: 10.1063/1.372996

[55] L. Del Bianco, F. Spizzo, Tian Li, R. Adhikari and A. Bonanni, *Phys. Chem. Chem. Phys.*, 2018, **20**, 25411. DOI: 10.1039/C8CP04475A

[56] D. Fiorani, A.M. Testa, F. Lucari, F. D'Orazio, H. Romero, *Physica B*, 2002, **320**, 122. DOI: 10.1016/S0921-4526(02)00659-2

[57] G.V. Samsonov 'The Oxide Handbook' IFI/PLENUM New York-Washington-London 1973. The density of bulk magnetite has been considered, despite the presence of Mn as dopant in the investigated NPs. The density of manganese ferrite MnF_2O_4 is 5.04 g/cm^3, very close to that of Fe_3O_4.

[58] E.C. Stoner and E.P. Wohlfarth, *IEEE Trans. Magn.*, 1991, **27**, 3475. DOI: 10.1109/TMAG.1991.1183750. The Stoner Wohlfarth model allows one to calculate the hysteresis loop of an assembly of single-domain NPs with uniaxial anisotropy, provided that they are magnetically non-interacting, which is not our case.

[59] One may object that we have overestimated the volume of the NPs by assuming that they are perfectly cubic. This possible overestimation can be, to some extent, offset by the fact that, as explained in Section 3.4, K_{eff}, which also enters in relation (2), is probably underestimated.

[60] R. Hergt and S. Dutz, *J. Magn. Magn. Mater.,* 2007, **311**, 187.
DOI: 10.1016/j.jmmm.2006.10.1156

[61] B. Mehdaoui, R.P. Tan, A. Meffre, J. Carrey, S. Lachaize, B. Chaudret and M. Respaud, *Phys. Rev. B,* 2013, **87**, 174419-1. DOI:10.1103/PhysRevB.87.174419

[62] N. S. Susan Mousavi, S. D. Khapli and S. Kumar, *J. Appl. Phys.*, 2015, **117**, 103907.
DOI: 10.1063/1.4914484

[63] E. Myrovali, N. Maniotis, A. Makridis, A. Terzopoulou, V. Ntomprougkidis, K. Simeonidis, D. Sakellari, O. Kalogirou, T. Samaras, R. Salikhov, M. Spasova, M. Farle, U. Wiedwald and M. Angelakeris, *Scientific Reports,* 2016, **6**, 37934. DOI: 10.1038/srep37934

[64] H. Mamiya and B. Jeyadevan, *Scientific Reports*, 2011, **1**, 157. DOI: 10.1038/srep00157

[65] Y. L. Raikher and V. I. Stepanov, *J. Magn. Magn. Mater.*, 2008, **320**, 2692. DOI: 10.1016/j.jmmm.2008.05.041

[66] P. Allia, M. Coisson, M. Knobel, P. Tiberto and F. Vinai, *Phys. Rev. B*, 1999, **60**, 12207.
DOI: 10.1103/PhysRevB.60.12207

[67] S. Signoretti, L. Del Bianco, L. Pasquini, G. Matteucci, C. Beeli and E. Bonetti, *J. Magn. Magn. Mater.*, 2003, **262**, 142. DOI: 10.1016/S0304-8853(03)00037-4

[68] S. Zhang, J. Li, G. Lykotrafitis, G. Bao and S. Suresh, *Adv. Mater.* 2009, **21**, 419. DOI: 10.1002/adma.200801393